A Triboelectric Energy Harvester Using Low-Cost, Flexible, and Biocompatible Ethylene Vinyl Acetate (EVA)

Faezeh Arab Hassani, *Member, IEEE*, and Chengkuo Lee, *Member, IEEE*

***Abstract*— In this paper, we propose a triboelectric energy harvester (EH) using ethylene vinyl acetate (EVA) polymer for the first time. EVA acts as a polymer with positive electrification properties against metals such as gold and aluminum. The EVA sheet provides us with a low-cost EH as the usage of already roll-to-roll-patterned sheet enables us to avoid the common expensive patterning methods for introducing the required roughness to the EH device. Moreover, the biocompatibility and flexibility of EVA makes it a suitable candidate for future implantation of this EH inside body. The transparency of EVA helps us to design the EVA-based EHs in different configurations for the characterization with two types of setups. The proposed new mass-tapping and detachment setups for the EVA EHs bring us more effective methods to quantitatively investigate important properties of EH while resembling the daily motions of a living being rather than using motorized characterization methods. [2014-0305]**

***Index Terms*— Bio-compatible, energy harvesting, flexible electronics, low cost, triboelectricity.**

I. Introduction

THE OPERATION of triboelectric nanogenerators (TENG) devices is based on contact electrification and electrostatic induction that is caused by two steps of contact and separation of triboelectric materials [1]–[3]. Usually the presented characterization setup includes a cyclic tapping with a constant force applied by using a shaker [4]–[6] that provides the opportunity for a quantitative study on the behavior of the device. However, this type of characterization may not resemble the daily motions of a living being in life. Body motion [7], hand tapping [8], walking [9], [10], touching [11], liquid wave energy [12], and wind [13] are the other common ways as more realistic methods for demonstrating the benefits of TENG devices but not suitable for a more detailed investigation on them. Apart from the characterization method for TENG devices, the main recent development for these devices is, the demonstration of high output power energy harvesters to replace common power sources [14]–[16]. The improvement of their characteristics requires the usage of expensive equipment for etching and patterning to introduce surface micro/nano-roughness [4], [17]–[20]. On the other hand, future application of these devices as implantable wireless sensors or power sources in body necessitates a careful choosing of triboelectric materials that are bio-compatible.

Various types of polymers are being used for TENG devices such as Polyethylene terephthalate (PET) [17], Polydimethylsiloxane (PDMS) [17], Kapton [14], Perfluoroalkoxy (PFA) [18], Polytetrafluoroethylene (PTFE) [4], and Nylon [2]. In order to accommodate these devices inside body people need to check non-degradability and biocompatibility [21]. Important factors like their poor biocompatibility, releasing degradation products, poor processability, and loss of mechanical properties make them unsuitable for in vivo biomedical applications [21]. PET, PDMS, Kapton, PFA, PTFE, and Nylon are all considered as non-degradable polymers for clinical applications [22]–[24]. Among these polymers, PDMS has been vastly used in drug delivery applications due to its biocompatibility [25]. Important to note that mild inflammatory reaction has been reported for PDMS when implanted [26], [27]. Moreover, PDMS is considered as a polymer with negative electrification properties for energy harvesting purposes [6], [17]. Nylon is considered as a triboelectric material with positive electrification properties; however it shows slight to severe tissue reaction after the implantation [28]. In this manuscript, we have used the commonly available Ethylene Vinyl Acetate (EVA) sheet as the new triboelectric material for the proposed energy harvester (EH). EVA is used in wide variety of biomedical applications including drug delivery systems and medical implants [23], [29], [30] with no inflammatory responses and good tissue compatibility [28]. Important to note that EVA as a hydrocarbon material shows slight positive electrification properties versus metals such as gold (Au) and Aluminum (Al) [31]. Previous works show that the increase of surface charge density and consequently output voltage of TENG device is achieved by introducing surface roughness to the triboelectric materials [4], [17]–[19]. Due to this fact, the existence of macro-patterned bumps on the surface of EVA sheet is expected to improve the output characteristics

Manuscript received October 7, 2014; revised December 27, 2014; accepted January 22, 2015. Date of publication March 4, 2015; date of current version September 29, 2015. This work was supported in part by the NRF2011 NRF-CRP001-057 Program entitled Self-Powered Body Sensor for Disease Management and Prevention-Orientated Healthcare through the National Research Foundation, Singapore, under Grant R-263-000-A27-281, and in part by the Faculty Research Committee through the National University of Singapore, Singapore, under Grant R-263-000-692-112. Subject Editor J. A. Yeh.

F. A. Hassani is with the Kroto Research Institute, University of Sheffield, Sheffield S10 2TN, U.K., and also with the Department of Electrical and Computer Engineering, National University of Singapore, Singapore 119077 (e-mail: f.a.hassani@sheffield.ac.uk).

C. Lee is with the Department of Electrical and Computerss Engineering, National University of Singapore, Singapore 119077 (e-mail: elelc@nus.edu.sg).

Color versions of one or more of the figures in this paper are available online at http://ieeexplore.ieee.org.

Digital Object Identifier 10.1109/JMEMS.2015.2403256

of EH. In brief, biocompatibility, large positive electrification property, and low-cost manufacturability in terms of roll-to-roll processing of millimeter-scale-patterned EVA sheets are the three driving factors for us to investigate EVA as a promising material for the triboelectric EH in our study.

We have presented three types of triboelectric EHs in this study. In the first type, an EVA sheet is used versus Al foil. For this EH, we have applied a "mass-tapping" setup in which an accelerometer is used for controlling the applied tapping force and quantitatively studying the output characteristics of EH. For the second type, a sheet of millimeter-scale-patterned EVA and an identical EVA sheet coated with a thin Au layer are assembled face-to-face with different degree of pattern-overlap as a new configuration of triboelectric EH with an initial narrow air-gap. Then a new "detachment" setup has been introduced for the second EH to investigate the detailed electrification mechanism associated with this new triboelectric EH configuration. The proposed mass-tapping and detachment setups in this paper help us to represent the daily motions in life such as hand touching of any type of touchscreens or trackpads, and gestures like clapping, respectively. The biocompatibility and flexibility of EVA pave the way for the future implantation of the EH under skin. The transparency of EVA sheet also allows us to align the bumps in the top and bottom substrates for optimizing the output characteristics of EH. The results indicate the millimeter-scale-patterned EVA sheet is a promising low-cost biocompatible triboelectric material. In order to find out the effect of using a polymer with negative electrification properties against EVA, the third type of EH is introduced by adding a layer of PDMS to the second type of EH.

II. Configurations of EVA Energy Harvesters

EVA is produced by copolymerization of Ethylene (C_2H_4) and Vinyl Acetate (VA) ($C_4H_6O_2$) [32]. The weight percent of VA usually varies from 0-40% [25]. EVA with the density of 0.926-0.976 g/cm^3 is available as a plastic, thermoplastic elastomer, and rubber depending on the VA content in the copolymer [32], [33]. The EVA is mainly recognized for its flexibility and toughness (even at low temperatures), adhesion characteristics and stress-cracking resistance [34]. Chemical structure of EVA copolymer is shown in Fig. 1 (a). In this work, we have used the available EVA liner sheets with millimeter scale-bump patterns. The dimensions of a bump and the distance between bumps are shown in Fig. 1 (b). The SEM image of the bump is shown in Fig. 1 (c), while Fig. 1 (d) shows the cross section of the bump using an optical microscope. Table I, summaries the dimensions and properties of the EH. The top surface of each bump defines the contact area, S_{bump}, in our calculations.

Polyvinyl acetate (PVAc) as a base component of EVA acts as a positive triboelectric material against Al and Au [31]. Also by considering EVA in the group of hydrocarbon materials, a similar positive triboelectric charge is assumed for it versus Al and Au. Three types of EHs are proposed in this work. For the first type, EVA is used versus Al foil as shown in the schematic in Fig. 1 (e). Then for the second type of EVA-based EH, a layer of EVA has been used as bottom

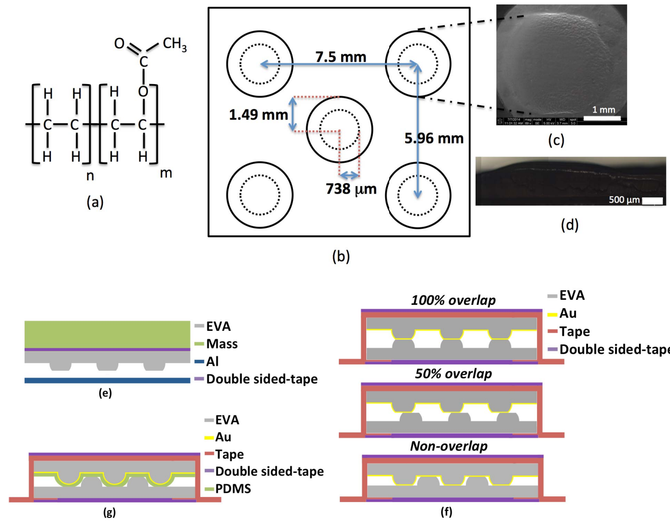

Fig. 1. (a) The chemical structure of an EVA copolymer, (b) a schematic on the EVA bump patterns on the EVA sheet and their dimensions, (c) the SEM top view of a bump, (d) the optical microscope image of the cross section of a bump, (e) the first type of EH featuring EVA versus Al, (f) the second type of EVA-based EHs in three different configurations featuring EVA versus Au, (g) the third type of EH featuring EVA versus PDMS.

TABLE I
Dimensions and Properties of Polymers Used for EHs

EVA Density (g/cm^3)		0.926-0.976
EVA permittivity (ε_{r1}) at 1 kHz [35]		2.65
EVA thickness at the center of bumps (d_{r1}) (μm)		820
Number of bumps (n) on the different	4 cm×6 cm	93
sizes of Au sputtered EVA substrate	2 cm×6 cm	62
	2 cm×2 cm	13.5
S_{bump} (mm^2)		1.71
C_{EH1} (pF) at z =0		2.27
C_{EH2} (pF) at z =0		4.54
C_{EH3} (pF) at z=0		9.09
PDMS permittivity (ε_{r2}) at 1 kHz [36]		2.65
PDMS thickness (d_{r2}) (μm)		200

substrate for the EH and on the other side a 100 nm of Au was sputter coated on the same kind of EVA. Taking advantage of the existence of bumps on EVA and Au sputtered EVA and the transparency of EVA, the bumps on top and bottom substrates can be aligned in a way that they completely overlap each other, *100% overlap*, overlap each other halfway, *50% overlap*, and do not cover each other, *non-overlap*. Figure 1 (f) shows the schematic of three configurations for EVA-based EHs. The third type of EH (Fig. 1 (g)) is prepared by spin coating a layer of PDMS onto the Au sputtered EVA of *non-overlap* EH named as *non-overlap PDMS*. In all the presented types of EHs, only a wire is taking out from the metal layer. A mass-tapping setup has been used to characterize the first type of EH while for the second and third types of EHs, a detachment setup has been proposed. The details on these setups are given later.

III. Investigation on the Output Characteristic of the First Type of EH Using "Mass-Tapping" Setup

An EVA layer with the size of 6 cm × 6 cm is attached using a double sided tape to a *Mass*. The *Mass* was used to model

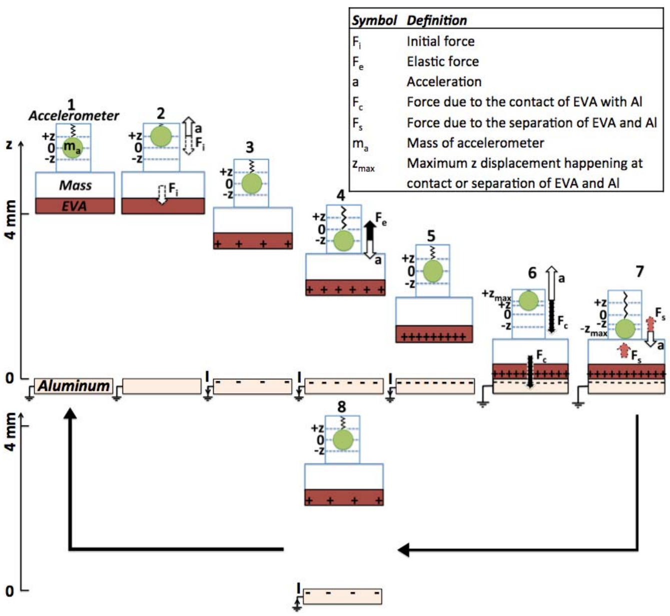

Fig. 2. Different steps of the mass-tapping experiment for the first type of EH.

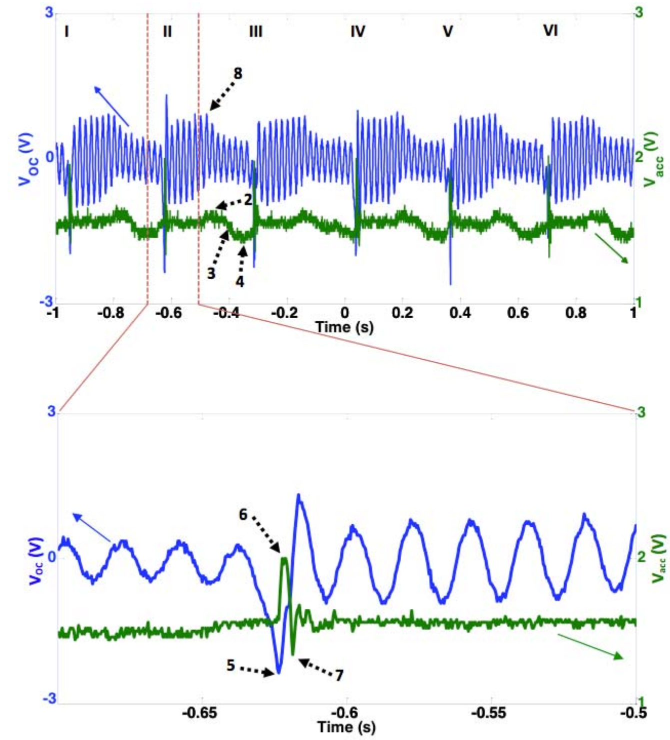

Fig. 3. V_{OC} and V_{acc} versus time for the first type of EH characterized by the mass-tapping setup.

different sizes of hand while clapping in the real life. The Mass was held by hand and it was tapped on the Al substrate that was attached on the stage. The number of bumps in contact with Al is 153. An ADXL325 accelerometer, with the typical sensitivity of 174 mV/g, is attached on top of the *Mass* as shown in step 1 of Fig. 2. The accelerometer is modeled using a mass, m_a, and a spring to present the movement of m_a in different steps of experiment. Figure 3 shows the open circuit voltage, V_{OC}, of devices and the relative accelerometer voltage, V_{acc}, versus time. Each step numbered in Fig. 2 is correlated with the numbers shown in Fig. 3.

The top EVA substrate in Fig. 2 is kept 4 mm away from the bottom Al substrate in step 1 and no charge is shown in EVA and Al layers. By bringing EVA nearer to Al substrates, the positive charge in EVA and negative charge in Al is increasing till reaching their highest values in step 6. In step 2 an initial force, F_i, is applied to the *Mass* to move it towards the Al substrate. A positive acceleration, a, is induced due to F_i in step 2. m_a starts to resonate due to the elastic force of spring that brings it from +z in step 2 to 0 in step 3, then −z in step 4 and 0 again in step 5. In step 5, the negative peak of V_{OC} happens as shown in the zoom view in Fig. 3. The negative peak of V_{OC} is matching with the shown direction of current, I, in step 5 of Fig. 3. The consistency between the sign of V_{OC} and I confirms the positive induced charge in EVA. During steps 2 to 5, a constant force is applying to the *Mass* for bringing it near to Al but as the velocity during these steps is constant no acceleration is caused by this force. In step 6, due to the sudden contact of *Mass* with the bottom stage, contact force, F_c, results in a sudden positive peak in acceleration. The total charge in step 6 is zero as the negative charge in Al is canceled out by positive charge in EVA. In step 7, the *Mass* is starting to be separated from Al so a negative peak is appeared for the acceleration. By separating EVA from Al, the negative charge in Al started to disappear and for this reason in step 8, a positive peak in V_{OC} is appeared.

TABLE II

CALCULATED VELOCITIES AND DISPLACEMENTS FOR THE FIRST TYPE OF EH CHARACTERIZED BY THE MASS-TAPPING SETUP AT THE NEGATIVE CONTACT PEAK OF V_{OC}

V_{OC} (V)	V_{acc} at t_6 (V)	a_{t6} (m/s^2)	t_6-t_5 (s)	v_{t5} (m/s)	Z_{t5} (μm)
2.36	2	24.78	0.0012	0.029	17.4
2.24	1.98	23.65	0.0012	0.028	16.8
2	2	24.78	0.0016	0.039	31.2
1.64	2.02	25.90	0.0016	0.041	32.8

Six times of the above mentioned contact-separation cycle in Fig. 2, by trying to keep the time interval between cycles, relatively constant, were done in 2 s of experiment as shown in cycles I-VI of Fig. 3. Considering one of the cycles in the zoom view in Fig. 3, the time interval between the negative peak of V_{OC}, t_5, and positive peak of acceleration, t_6, will be used for calculating the velocity at the negative peak of V_{OC}.

$$a_{t6} = \frac{|v_{t6} - v_{t5}|}{t_6 - t_5} \tag{1}$$

where $v_{t6} = 0$. a_{t6} is calculated by dividing (V_{acc}−1.56 V) to the sensitivity of accelerometer (174 mV/g). Noting that 1.56 V is due to the DC biasing of accelerometer and g=9.8 m/s^2. Then the distance of EVA from Al, z_{t5}, where the negative triboelectric peak happens can be calculated by:

$$z_{t5} = \frac{v_{t6} + v_{t5}}{2}(t_6 - t_5) \tag{2}$$

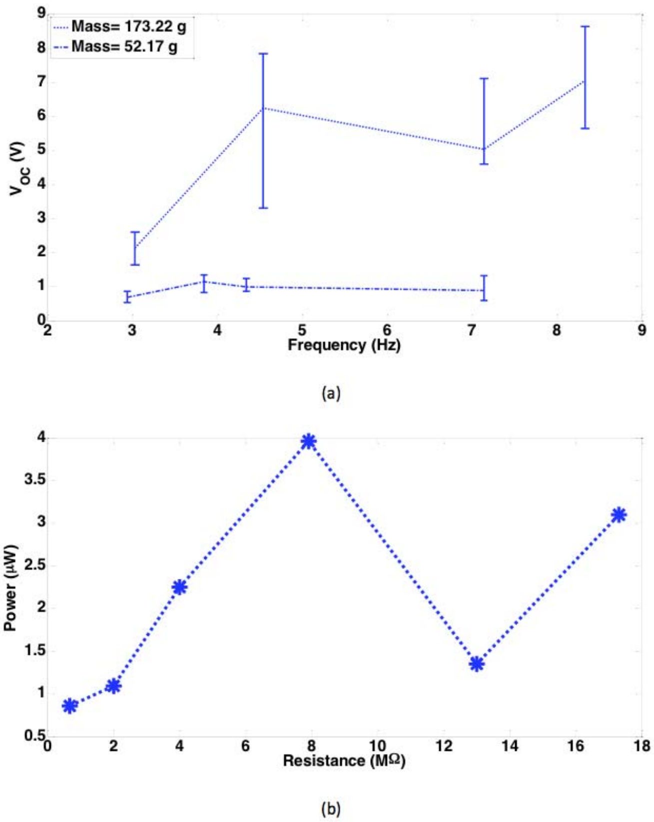

Fig. 4. (a) V_{OC} versus frequency for the first type of EH with different *Masses*, (b) power versus load resistance for the EH with 173.22 g *Mass*.

Table II shows the calculated velocities and displacements at 4 cycles (II, III, IV, VI) in Fig. 3. In the other two cycles (I, V) among the above mentioned six cycles, due to the delay in the response of accelerometer, the negative peak of V_{OC} is happening after the positive peak of acceleration. For this reason they are not used for the calculations in Table II. By increasing the tapping frequency, more number of cycles out of the total cycles in 2 s faces the accelerometer's delay. Changing of velocity affects V_{OC} [2], [37] and the variation in velocity values in 4 cycles results in different V_{OC} values. We expected to see higher V_{OC} values for higher v_{t5} but for small velocity values with small changes shown in Table II, it is not easy to match the values of v_{t5} with the values of V_{OC}. Important to note that, for one order of magnitude larger velocities, the increase in V_{OC} values is visible. This fact is discussed later in section IV.

Two different Masses of 173.22 g and 52.17 g are used in our experiment to study the effect of applied force due to the *Mass* on EH. Fig. 4 (a) shows V_{OC} versus frequency for two different *Masses*. Smaller weight of mass leads to smaller V_{OC}. The wider error bars especially at higher frequencies in Fig. 4 (a) are due to the variation of velocity at the negative peak of V_{OC} as previously explained. For calculating the level of output power of EH, a range of load resistances is applied at the output of EH. The maximum output power happens at the matching load resistance with the impedance of EH. The power of EH for 173.22 g *Mass* versus different load resistances at the frequency of ∼3 Hz is shown in Fig. 4 (b). To investigate the detailed electrification mechanism and improve the output power of EH, the EVA sheet assembled with the Au-coated EVA sheet in the configuration of Fig.1 (f) and (g) is characterized in the next section by using a new "detachment" setup where a narrow air gap between top and bottom substrates, i.e., the EVA sheet surface, and higher applied force are introduced.

IV. Investigation on the Output Characteristic of EVA-Based EH Using "Detachment" Setup

In order to achieve high power for the EH, keeping a narrow airgap, i.e., a minimum distance, between top and bottom substrates during the contact and separation steps provides a larger equivalent capacitance for EH. As a result, smaller impedance leads to higher output current for EH [37]. Due to this factor, a new detachment set up is presented here for the EVA-based EH to improve the output power as well as its output voltage. The relationship between output voltage of the EH, V, and its equivalent capacitance, C_{EH}, and open circuit voltage, V_{OC}, is shown in (1) [37]:

$$V = \frac{-1}{C_{EH}} Q + V_{OC} \tag{3}$$

where Q is the induced charge on the conducting Au layer. V_{OC} and C_{EH} are calculated as:

$$V_{OC} = \frac{\sigma z}{\varepsilon_0} \tag{4}$$

$$C_{EH} = \frac{\varepsilon_0 S}{d_0 + z} \tag{5}$$

where σ is the surface charge density, $d_0 = d_{r1}/\varepsilon_{r1}$, where ε_{r1} and d_{r1} are the permittivity and thickness of EVA layer, respectively, z is the distance between Au and EVA substrates, the vacuum permittivity, ε_0, is 8.85×10^{-12}, and S is the contact area.

To fulfill the above mentioned criterion for keeping air gap z at its minimum value, top and bottom 4 cm × 4 cm substrates are taped together and then they are assembled using a double sided tape on the stage. The whole device is then covered with a tape on the stage to make sure of stability of the device on the stage. Finger tapping is used to characterize these EHs but we have used an ADXL325 accelerometer to keep the applied force constant throughout the experiment steps. The accelerometer was attached on hand and the output voltage of the accelerometer in z-axis was displayed on one channel of oscilloscope while the other channel displays the triboelectric output voltage of EH. However, the uncertainty of manually keeping a constant force motivated us to use a different way. In our new method, a layer of double sided tape is completely covered the top of EH and finger tapping is done using a latex glove on top of the double sided tape. The characterization setup is shown in Fig. 5 (a). As the adhesion of the glove to the double sided tape is constant, we have more control on keeping the acceleration and consequently the force constant. Moreover, using the double sided tape a higher level of separation force, "detachment force", is applied to EH. The applied force of finger tapping is measured using a force gauge. Direct finger tapping on the stage of the

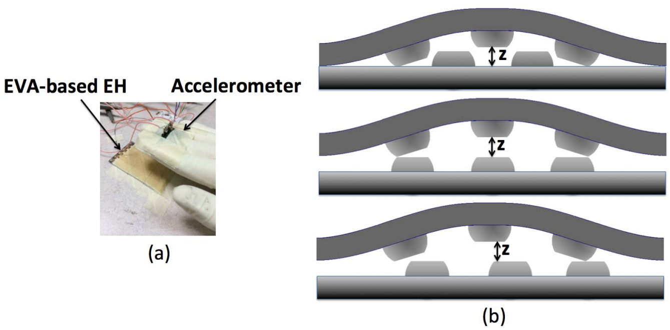

Fig. 5. (a) The detachment setup, (b) the schematic for z-displacement in three configurations of EVA-based EHs.

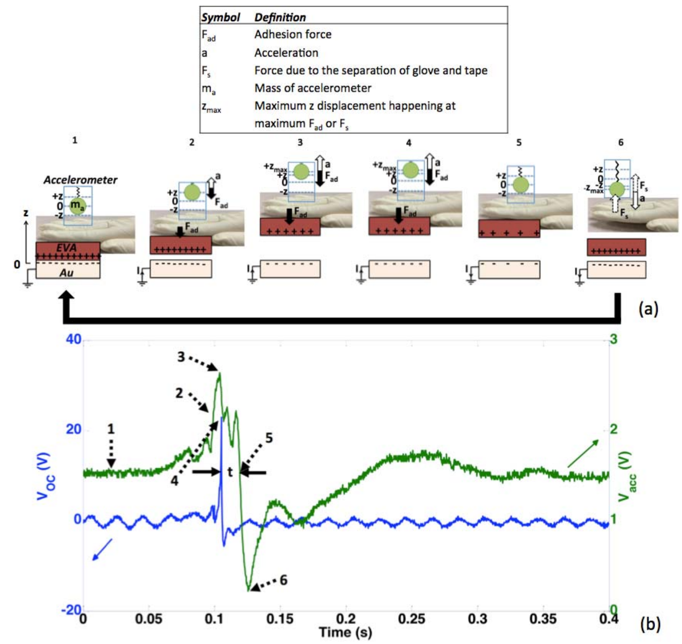

Fig. 6. (a) Different steps of detachment experiment for the three configurations of EVA-based EHs and *non-overlap PDMS* EH, (b) V_{OC} and V_{acc} versus time for the *non-overlap* EVA-based EH characterized by using the detachment setup.

force gauge shows the applied force of 3 N. When a double sided-tape was stuck onto the stage of the force gauge, the applied finger tapping force was increased to more than 9 N. By applying the detachment force the separation distance reached its maximum value due to the flexibility of the top EVA substrate. By using the detachment method we only focus on the separation step of triboelectric materials for the quantitative investigation on the output power of EH.

As shown in Fig. 1 (f), three configurations are considered for the EVA-based EH by aligning the bumps on top and bottom substrates. If n is the number of bumps on Au substrate, *n/2*, *n* and *2n* are the number of bumps in contact between EVA and Au substrates in *50% overlap*, *100% overlap* and *non-overlap*, respectively. The following equations present the equivalent C_{EH} for each configuration:

$$C_{EH1} = \frac{n}{2}\frac{\varepsilon_0 S_{bump}}{\frac{d_{r1}}{\varepsilon_{r1}} + z_1} \quad (50\%\ overlap) \tag{6}$$

$$C_{EH2} = n\frac{\varepsilon_0 S_{bump}}{\frac{d_{r1}}{\varepsilon_{r1}} + z_1} \quad (100\%\ overlap) \tag{7}$$

$$C_{EH3} = 2n\frac{\varepsilon_0 S_{bump}}{\frac{d_{r1}}{\varepsilon_{r1}} + z_1} \quad (Non\text{-}overlap) \tag{8}$$

If we consider the same displacement of top substrate for all three configurations during the experiment, we will have $z_1 = z_2 = z_3 = z$ as shown in Fig. 5 (b). As a result the value of C_{EH} for each configuration is only related to the number of bumps in contact and $C_{EH1} < C_{EH2} = 2C_{EH1} < C_{EH3} = 4C_{EH1}$.

The maximum output power for the EH is achieved in case that the load resistance value is matching with the impedance of C_{EH} for each EH. Due to this fact, the *non-overlap* EH with the highest C_{EH} value should show higher output power due to its lower impedance. Higher number of bumps also leads to the increase of induced surface triboelectric charges and larger V_{OC}. The following experiments are carried out to confirm these tendencies for C_{EH} by using the output power of the device and V_{OC} for all three configurations. The values of C_{EH} for all the three configurations are presented in Table I.

As previously mentioned in this section, to study the effect of misalignment of bumps on top and bottom substrates on the output characteristics of EH, the Au substrate is kept fixed while the EVA substrate is moving, in order to achieve half-overlap, fully overlap and non-overlap configurations in Fig. 1 (f). Fig. 6 (a) shows the steps 1 to 6 for the appearance of triboelectric charges in EVA and Au by changes in z displacement as well as their corresponding accelerations in each step. The real time V_{OC} and V_{acc} of *non-overlap* configuration is shown in Fig. 6 (b) and each step of Fig. 6 (a) is labeled in Fig. 6 (b). Step 1 shows full contact of EVA and Au with the induced triboelectric charges in their surface. The total charge value in this step is zero. In step 2, the adhesion force, F_{ad}, of glove to the double sided tape induces a positive acceleration in accelerometer and EVA and Au substrate are started to become separated. As the distance between EVA and Au is increased in this step, the current is applied, in opposite direction of current in steps 3 to 5 in Fig. 2, to cancel the negative charge in Au. In step 3, the glove is started to be separated from tape so the EH experiences the maximum F_{ad} and acceleration due to this force. The distance between EVA and Au is still increasing due to the adhesion of glove that increases the current in step 4 even though by slightly separation of glove from the tape, F_{ad} starts to vanish. In this step the highest distance between EVA and Au achieved that causes a negative peak in V_{OC}. The matching of direction of current with the positive sign of V_{OC} confirms the positive induced charge in EVA. This fact is consistent with the negative sign of V_{OC} in the contact step of mass-tapping. In step 5 the glove is almost separated and accelerometer faces a zero velocity at this point. Due to the reduction of distance between EVA and Au the sign of current is changed in this step to be able to increase the negative charge in Au. The negative peak of V_{OC} happens before step 5 but it is not labeled in Fig. 6 (a) as the focus of this setup is on the detachment peak of V_{OC}. The positive peak of V_{acc} shows

TABLE III
CALCULATED VELOCITIES AND DISPLACEMENTS FOR THE NON-OVERLAP EVA-BASED EH CHARACTERIZED BY DETACHMENT SETUP AT THE POSITIVE DETACHMENT PEAK OF V_{OC}

Type of EVA-based EH	V_{OC} (V)	V_{acc} at t_4 (V)	a_{t4} (m/s^2)	t_5-t_4 (s)	v_{t4} (m/s)	Z_{t5} (μm)
50% overlap	12.4	2.4	47.31	0.014	0.66	34.8
100% overlap	19.2	2.66	61.95	0.0142	0.87	33.6
Non-overlap	23	2.4	47.31	0.014	0.66	62.4

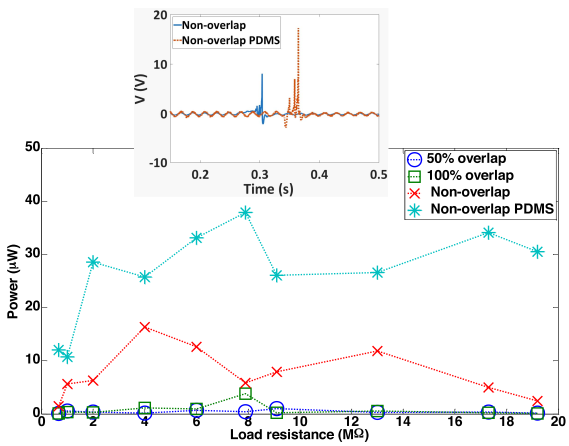

Fig. 7. Power versus load resistances for *50% overlap*, *100% overlap*, *non-overlap*, and *non-overlap PDMS* EVA-based EHs, inset: Output voltage versus time for the *non-overlap PDMS* and *non-overlap* EHs at their matching load resistances.

the strength of adhesion of glove to the substrate. By using the time interval between the V_{acc} time in step 4, t_4, and V_{OC} time in step 5, t_5, the velocity and z-displacement in the detachment phase of EH, z_{t4}, can be calculated as following:

$$a_{t4} = \frac{|v_{t4} - v_{t5}|}{|t_4 - t_5|} \tag{9}$$

where $v_{t5} = 0$.

$$z_{t4} = \frac{v_{t4} + v_{t5}}{2}(t_5 - t_4) \tag{10}$$

Table III shows the detachment velocity and z-displacement for three configurations of EVA-based EH. a_{t4} is calculated same as a_{t6} in section III. The values of velocity in the detachment setup is one order of magnitude larger that velocities in Table II. Due to this fact, V_{OC} values in Table III are larger than V_{OC} values in Table II.

The output power versus a range of load resistances for three configurations is shown in Fig. 7. As shown in Fig. 7, the *non-overlap* configuration shows the highest output power due to its lowest impedance that is consistent with the assumption of highest C_{EH} for this configuration. Figure 7 shows that the optimum load resistance, at which the peak of power occurs, is reduced from 9.1 MΩ for the *50% overlap* EH to 7.9 MΩ for the *100% overlap* EH, and 4 MΩ for the *non-overlap* EH, that is matching with the respective calculated C_{EH} values for these EHs in Table I. In order to further enhance the output power of the *non-overlap* EH, using of a polymer with negative electrification properties such as PDMS [6], [17] against EVA increases the electronegativity difference between these two triboelectric polymers that leads to higher value of σ and consequently higher value of V_{OC} with respect to eq. (4). For this reason, a 200 μm-layer of PDMS is coated on Au sputtered EVA in *non-overlap PDMS* configuration (Fig. 1 (g)). For the preparation of this device, PDMS is mixed with the reticulating agent with the ratio of 10:1 and stirred for 3-4 minutes. Thirty minutes of degassing was done for the mixture in a vacuum desiccator. Then the mixture is spin coated at the speed of 500 rpm for 5 s on Au sputtered EVA. The sample is baked afterwards for 30 minutes at 90 °C. The PDMS substrate is then measured versus EVA by using the same detachment setup that was used for all the three configurations of EVA-based EHs in Fig. 7. The output power of *non-overlap PDMS* EH is compared with the output characteristics of the three configurations of EVA-based EHs in Fig. 7. For the *non-overlap PDMS* EH, $d_0 = d_{r1}/\varepsilon_{r1} + d_{r2}/\varepsilon_{r2}$, where d_{r2} and ε_{r2} are the thickness of PDMS layer and its dielectric constant, respectively. By assuming that, the number of bumps in contact between the EVA and Au substrates for the *non-overlap PDMS* EH is $2n$, same as the *non-overlap* EH, the C_{EH} value for this EH, C_{EH4}, is 7.31 pF. Smaller value of C_{EH4} than C_{EH3} causes higher value of impedance that was expected to result in a smaller output power for the *non-overlap PDMS* EH compared to the *non-overlap* EH. The peak of output power for the *non-overlap PDMS* EH is happening at the matching load resistance of 7.9 MΩ that is larger than that of the *non-overlap* EH and is consistence with the calculated C_{EH} value for this EH, but its output power is two times higher than that of the *non-overlap* EH. This is due to the higher output voltage for the *non-overlap PDMS* EH in comparison with the output voltage of other configuration of EHs. The output voltage versus time for the *non-overlap PDMS* EH at the matching load resistance of 7.9 MΩ and for the *non-overlap* EH at 4 MΩ are shown in inset of Fig. 7. The maximum V of 17.3 V has been achieved for the *non-overlap* EH while the non-overlap EH shows the output voltage of 8.08 V.

TABLE IV
MEASURED V_{OC} VALUES OF *50% Overlap*, *100% Overlap*, *Non-Overlap*, AND *Non-Overlap PDMS* EVA-BASED EHs

Type of EVA-based EH	V_{OC}		
	No. 1	No. 2	No. 3
50% overlap	7.4	2.26	12.4
100% overlap	5.6	3.8	19.2
Non-overlap	16.2	19.7	23
Non-overlap PDMS	24.6	27	31

Table IV shows the V_{OC} measured for three times for the three configurations of EVA-based devices as well as *non-overlap PDMS* EH. V_{OC} is increased by increasing the number of contact bumps from *50% overlap* to the *non-overlap* configuration as presented in Table IV.

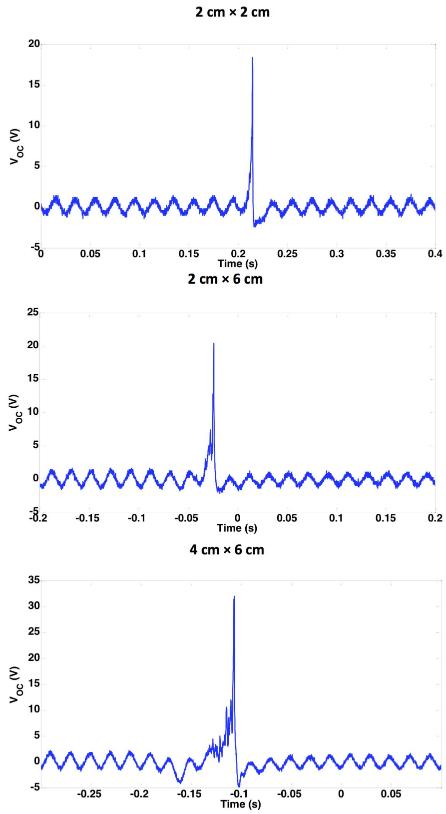

Fig. 8. V_{OC} versus time for different sizes of the *non-overlap* EH.

Furthermore, *non-overlap PDMS* EH shows a larger value of V_{OC} due to the higher electronegativity difference between EVA and PDMS in comparison with EVA and Au as the triboelectric pair in the *non-overlap EH*.

The size of EH in the *non-overlap* configuration, with the highest output voltage in Table IV, is scaled down to study the effect of dimensions on V_{OC} of EHs. Figure 8 shows that V_{OC} is increased when the sample size increases from 2 cm × 2 cm to 4 cm × 6 cm. The V_{OC} is more than 30 V for the 4 cm × 6 cm sample at the testing acceleration of 60 m/s^2. More bending of top substrate in 4 cm × 6 cm device as well as higher number of bumps causes higher V_{OC} for the larger device.

V. Conclusion

In this paper, we have presented a triboelectric energy harvester made of Ethylene Vinyl Acetate as the triboelectric polymer with positive electrification properties for the first time. EVA has been examined versus Au and Al with different electronegativities to confirm the positive induced charge in EVA as expected. The usage of roll-to-roll processed macro-patterned EVA sheet for the EH leads to a very low cost EH without the need of applying extra equipment for patterning its surface. Biocompatibility and flexibility of EVA sheet paves the way for the future implantation of this device under skin. Moreover, the transparency of EVA helped us to design the EH in different configurations for further optimization of output characteristics of the device. Two new characterization setups have been demonstrated in this paper to investigate important factors such as velocity and distance between top and bottom substrates at the separation or contact step of the experiment. Maximum open circuit voltage of 31 V and output power of 40 μW has been achieved for the EVA-based energy harvester with area of 4 cm × 6 cm. Higher values of detachment velocity and consequently acceleration achieved by using the detachment setup result in one order of magnitude larger V_{OC} for the characterized devices in comparison with the contact velocity and acceleration values achieved by using the mass-tapping setup.

References

[1] S. Wang, Y. Xie, S. Niu, L. Lin, and Z. L. Wang, "Freestanding triboelectric-layer-based nanogenerators for harvesting energy from a moving object or human motion in contact and non-contact modes," *Adv. Mater.*, vol. 26, no. 18, pp. 2818–2824, 2014.

[2] S. Wang, L. Lin, Y. Xie, Q. Jing, S. Niu, and Z. L. Wang, "Sliding-triboelectric nanogenerators based on in-plane charge-separation mechanism," *Nano Lett.*, vol. 13, no. 5, pp. 2226–2233, Apr. 2013.

[3] F.-R. Fan, Z.-Q. Tian, and Z. L. Wang, "Flexible triboelectric generator," *Nano Energy*, vol. 1, no. 2, pp. 328–334, Mar. 2012.

[4] J. Chen *et al.*, "Harmonic-resonator-based triboelectric nanogenerator as a sustainable power source and a self-powered active vibration sensor," *Adv. Mater.*, vol. 25, no. 42, pp. 6094–6099, 2013.

[5] X.-S. Zhang *et al.*, "High-performance triboelectric nanogenerator with enhanced energy density based on single-step fluorocarbon plasma treatment," *Nano Energy*, vol. 4, pp. 123–131, Mar. 2014.

[6] L. Dhakar, F. E. H. Tay, and C. Lee, "Investigation of contact electrification based broadband energy harvesting mechanism using elastic PDMS microstructures," *J. Micromech. Microeng.*, vol. 24, no. 10, p. 104002, Sep. 2014.

[7] H. Zhang, Y. Yang, T.-C. Hou, Y. Su, C. Hu, and Z. L. Wang, "Triboelectric nanogenerator built inside clothes for self-powered glucose biosensors," *Nano Energy*, vol. 2, no. 5, pp. 1019–1024, 2014.

[8] Y. Zheng *et al.*, "An electrospun nanowire-based triboelectric nanogenerator and its application in a fully self-powered UV detector," *Nanoscale*, vol. 6, no. 14, pp. 7842–7846, May 2014.

[9] T.-C. Hou, Y. Yang, H. Zhang, J. Chen, L.-J. Chen, and Z. L. Wang, "Triboelectric nanogenerator built inside shoe insole for harvesting walking energy," *Nano Energy*, vol. 2, no. 5, pp. 856–862, Mar. 2013.

[10] X. Cheng, B. Meng, X. Zhang, M. Han, Z. Su, and H. Zhang, "Wearable electrode-free triboelectric generator for harvesting biomechanical energy," *Nano Energy*, vol. 12, pp. 19–25, Mar. 2015.

[11] Y. Yang *et al.*, "Electret film-enhanced triboelectric nanogenerator matrix for self-powered instantaneous tactile imaging," *ACS Appl. Mater. Interf.*, vol. 6, no. 5, pp. 3680–3688, 2014.

[12] Z.-H. Lin, G. Cheng, L. Lin, S. Lee, and Z. L. Wang, "Water-solid surface contact electrification and its use for harvesting liquid-wave energy," *Angew. Chem. Int. Ed. English*, vol. 52, no. 48, pp. 12545–12549, 2013.

[13] Y. Xie *et al.*, "Rotary triboelectric nanogenerator based on a hybridized mechanism for harvesting wind energy," *ACS Nano*, vol. 7, no. 8, pp. 7119–7125, Jun. 2013.

[14] S. Wang *et al.*, "Motion charged battery as sustainable flexible-power-unit," *ACS Nano*, vol. 7, no. 12, pp. 11263–11271, Nov. 2013.

[15] G. Zhu *et al.*, "Toward large-scale energy harvesting by a nanoparticle-enhanced triboelectric nanogenerator," *Nano Lett.*, vol. 13, no. 2, pp. 847–853, 2013.

[16] J. Yang *et al.*, "Broadband vibrational energy harvesting based on a triboelectric nanogenerator," *Adv. Energy Mater.*, vol. 4, no. 6, pp. 1–9, Apr. 2014.

[17] F.-R. Fan, L. Lin, G. Zhu, W. Wu, R. Zhang, and Z. L. Wang, "Transparent triboelectric nanogenerators and self-powered pressure sensors based on micropatterned plastic films," *Nano Lett.*, vol. 12, no. 6, pp. 3109–3114, 2012.

[18] Y. Su *et al.*, "Fully enclosed cylindrical single-electrode-based triboelectric nanogenerator," *ACS Appl. Mater. Interf.*, vol. 6, no. 1, pp. 553–559, 2014.

[19] M.-L. Seol, J.-H. Woo, D.-I. Lee, H. Im, J. Hur, and Y.-K. Coi, "Nature-replicated nano-in-micro structures for triboelectric energy harvesting," *Small*, vol. 10, no. 19, pp. 3887–3894, 2014.

[20] L. Dhakar, F. E. H. Tay, and C. Lee, "Development of a broadband triboelectric energy harvester with SU-8 micropillars," *J. Microelectromech. Syst.*, vol. 24, no. 1, pp. 91–99, Feb. 2015.
[21] P. A. Gunatillake and R. Adhikari, "Biodegradable synthetic polymers for tissue engineering," *Eur. Cells Mater.*, vol. 5, pp. 1–16, May 2003.
[22] P. J. Rousche, D. S. Pellinen, D. P. Pivin, J. C. Williams, R. J. Vetter, and D. R. Kipke, "Flexible polyimide-based intracortical electrode arrays with bioactive capability," *IEEE Trans. Biomed. Eng.*, vol. 48, no. 3, pp. 361–371, Mar. 2001.
[23] A. Subramaniam and S. Sethuraman, "Biomedical applications of nondegradable polymers," in *Natural and Synthetic Biomedical Polymers*. Amsterdam, The Netherlands: Elsevier, 2014, pp. 301–307.
[24] A. S. Breitbart and V. J. Ablaza, "Implant materials," in *Grabb and Smith's Plastic Surgery*. Baltimore, MD, USA: Williams & Wilkins, 2007, pp. 58–65.
[25] F. Yao and W. J. Kao, "Drug release kinetics and transport mechanisms of non-degradable and degradable polymeric delivery systems," *Expert Opinion Drug Del.*, vol. 7, no. 4, pp. 429–444, Apr. 2010.
[26] M. W. Toepke and D. J. Beebe, "PDMS absorption of small molecules and consequences in microfluidic applications," *Lab Chip*, vol. 6, no. 12, pp. 1484–1486, 2006.
[27] J. Wang, C. J. Bettinger, R. S. Langer, and J. T. Borenstein, "Biodegradable microfluidic scaffolds for tissue engineering from amino alcohol-based poly(ester amide) elastomers," *Organogenesis*, vol. 6, no. 4, pp. 212–216, 2010.
[28] J. Park and R. S. Lakes, "Tissue response to implants," in *Biomaterials*. New York, NY, USA: Springer, 2007, pp. 265–290.
[29] P. Tallury, N. Alimohammasi, and S. Kalachandra, "Poly(ethylene-co-vinyl acetate) copolymer matrix for delivery of chlorhexidine and acyclovir drugs for use in the oral environment: Effect of drug combination, copolymer composition and coating on the drug release rate," *Dental Mater.*, vol. 23, no. 4, pp. 404–409, 2007.
[30] D. S. Hsieh, W. D. Rhine, and R. Langer, "Zero-order controlled-release polymer matrices for micro- and macromolecules," *J. Pharmaceutical Sci.*, vol. 72, no. 1, pp. 17–22, 1983.
[31] A. F. Diaz and R. M. Felix-Navarro, "A semi-quantitative tribo-electric series for polymeric materials: The influence of chemical structure and properties," *J. Electrostatics*, vol. 62, no. 4, pp. 277–290, 2004.
[32] I. O. Salyer and A. S. Kenyon, "Structure and property relationships in ethylene–vinyl acetate copolymers," *J. Polym. Sci., A-1, Polym. Chem.*, vol. 9, no. 11, pp. 3083–3103, 1971.
[33] B. John, K. T. Varughese, Z. Oommen, P. Pötschke, and S. Thomas, "Dynamic mechanical behavior of high-density polyethylene/ethylene vinyl acetate copolymer blends: The effects of the blend ratio, reactive compatibilization, and dynamic vulcanization," *J. Appl. Polym. Sci.*, vol. 87, no. 13, pp. 2083–2099, 2003.
[34] A. Rizvi, N. Chen, and C. B. Park, "Study on the mechanical properties of crosslinked EVA foams," presented at the Plastics, Annual Technical Conference, 2011.
[35] C. Vasile and M. Pascu, *Practical Guide to Polyethylene*. Shrewsbury, U.K.: Rapra Technology Ltd., 2005.
[36] R. S. Lima, T. P. Segato, A. L. Gobbi, W. K. Coltro, and E. Carrilho, "Doping of a dielectric layer as a new alternative for increasing sensitivity of the contactless conductivity detection in microchips," *Lab Chip*, vol. 11, no. 24, pp. 4148–4151, 2011.
[37] S. Niu *et al.*, "Simulation method for optimizing the performance of an integrated triboelectric nanogenerator energy harvesting system," *Nano Energy*, vol. 8, pp. 150–156, Sep. 2014.

Faezeh Arab Hassani (S'06–M'12) received the M.Sc. degree in electronics engineering from the University of Tehran, Tehran, Iran, in 2008, and the Ph.D. degree in electronics engineering from the University of Southampton, Southampton, U.K., in 2012. She joined the Japan Advanced Institute of Science and Technology, Nomi, Japan, for her Japan Society for the Promotion of Science (JSPS) Post-Doctoral Research Fellowship. In 2013, she joined the Department of Electrical and Computer Engineering, National University of Singapore, Singapore, as a Research Fellow. She is currently a Post-Doctoral Research Associate with the University of Sheffield, Sheffield, U.K. Her research interests include nanoelectronics and micro/nanoelectromechanical hybrid devices, sensors, and energy harvesting.

Chengkuo Lee (S'93–M'96) received the M.S. degree in materials science and engineering from National Tsing Hua University, Hsinchu, Taiwan, in 1991; the M.S. degree in industrial and system engineering from Rutgers University, New Brunswick, NJ, USA, in 1993; and the Ph.D. degree in precision engineering from the University of Tokyo, Tokyo, Japan, in 1996. He was a Foreign Researcher with the Nanometer Scale Manufacturing Science Laboratory, Research Center for Advanced Science and Technology, University of Tokyo, from 1993 to 1996. He was with the Mechanical Engineering Laboratory, AIST, MITI, Tsukuba, Japan, as a JST Research Fellow, in 1996. Thereafter, he became a Senior Research Staff Member with the Microsystems Laboratory, Industrial Technology Research Institute, Hsinchu. In 1997, he joined Metrodyne Microsystem Corporation, Hsinchu, and established the MEMS Device Division and the first micromachining fab for commercial purposes in Taiwan. He was the Manager of the MEMS Device Division from 1997 to 2000. He was an Adjunct Assistant Professor with the Electrophysics Department, National Chiao Tung University, Hsinchu, in 1998, and the Institute of Precision Engineering, National Chung Hsing University, Taichung, Taiwan, from 2001 to 2005. In 2001, he co-founded Asia Pacific Microsystems, Inc., where he first became the Vice President of Research and Development before becoming as the Vice President of the Optical Communication Business Unit and a Special Assistant to the Chief Executive Officer in charge of international business and technical marketing for the microelectromechanical systems (MEMS) foundry service. From 2006 to 2009, he was a Senior Member of the Technical Staff with the Institute of Microelectronics, A-STAR, Singapore. He is currently an Associate Professor with the Department of Electrical and Computer Engineering, National University of Singapore, Singapore. He has co-authored the book *Advanced MEMS Packaging* (McGraw-Hill, 2010). He has contributed to more than 200 international conference papers and extended abstracts, and 166 peer-reviewed international journal articles in the fields of sensors, actuators, energy harvesting, MEMS, nanoelectromechanical systems, nanophotonics, and nanotechnology. He holds nine U.S. patents.